

# Comparison of small ELM characteristics and regimes in Alcator C-Mod, MAST and NSTX

R. Maingi<sup>1</sup>, A.E. Hubbard<sup>2</sup>, H. Meyer<sup>3</sup>, J.W. Hughes<sup>2</sup>, A. Kirk<sup>3</sup>,  
R. Maqueda<sup>4</sup>, J.L. Terry<sup>2</sup> and the Alcator C-Mod, MAST and NSTX teams

<sup>1</sup> Oak Ridge National Laboratory, Oak Ridge, TN 37831, USA

<sup>2</sup> Massachusetts Institute of Technology, Cambridge, MA 02139, USA

<sup>3</sup> EURATOM/CCFE Culham, Culham, UK

<sup>4</sup> Princeton Plasma Physics Laboratory, Princeton, NJ 08543, USA

E-mail: [rmaingi@pppl.gov](mailto:rmaingi@pppl.gov)

Received 4 September 2010, accepted for publication 20 April 2011

Published 20 May 2011

Online at [stacks.iop.org/NF/51/063036](http://stacks.iop.org/NF/51/063036)

## Abstract

We report on the status of a set of ITPA-coordinated experiments between the Alcator C-Mod, MAST and NSTX devices to compare the characteristics and access conditions of discharges with small edge-localized modes (ELMs). The small ELMs in C-Mod, MAST and one of the two small ELM types in NSTX exist when  $\beta_{\text{ped}}^{\text{pol}}$  approached 10–15%, although the lower/upper limits of the operational windows differ. These small ELM regimes appear in diverted configurations very close to balanced double-null in each device. We classify these small ELMs as type II, based on the published characteristics from a number of previous studies. In addition, these type II ELMs in each device had multiple filaments with propagation in the co- $I_p$  or ion diamagnetic drift direction. Moreover, we conclude that these type II ELMs are distinct from the type V ELMs routinely observed in NSTX, which have one or two filaments and propagate in the electron diamagnetic drift direction.

(Some figures in this article are in colour only in the electronic version)

## 1. Introduction

Periodic eruptions from the plasma periphery have been observed since the discovery of the high-confinement mode (H-mode) regime in tokamaks [1]. These ejections are termed edge-localized modes (ELMs) [2], and one measure of the severity of ELMs is the fractional stored energy loss,  $\Delta W/W_{\text{tot}}$  where  $\Delta W$  is the energy loss and  $W_{\text{tot}}$  is the total plasma stored energy prior to the ELM. While the best plasma energy confinement is often correlated with large (type I) ELMs with  $\Delta W/W_{\text{tot}}$  up to 0.1–0.15 per ELM [3], such large transient heat pulses are usually exhausted to the divertor targets, leading to erosion and target lifetime reduction [4]. Given a typical ratio of pedestal stored energy ( $W_{\text{ped}}$ ) to  $W_{\text{tot}}$  of 0.3, the largest ELMs could exhaust between 0.33 and 0.5 of  $W_{\text{ped}}$ . Thus small ELM scenarios, e.g. with  $\Delta W/W_{\text{tot}} \leq 0.015$  ( $\Delta W/W_{\text{ped}} < 0.05$ ) per ELM, are being studied in many tokamaks and have commanded broad community interest [5–11], particularly those small ELM regimes with good energy confinement. In this paper, we use ‘small ELMs’ to denote those that have an indistinguishable effect on the stored energy outside of the typical 1–1.5% statistical error bar associated with equilibrium

reconstruction. These include type II ELMs that are observed with enhanced shaping or near double-null configuration [5–7], ‘grassy’ ELMs [10–12] observed at high poloidal  $\beta$  in JT-60U, small ELMs observed at high  $\beta$  in Alcator C-Mod [13], and type V ELMs observed over a wide operating range [14] in NSTX.

The urgency for development of small and no ELM scenarios has increased with the recent revision of the allowable ELM size in ITER to 1 MJ, representing about 0.3% of the 350 MJ plasma stored energy [15]. Two approaches to actively mitigate large type I ELMs being tested in the community include the use of resonant magnetic perturbations (RMPs) [16] and pellet pace-making [17]. In addition, assessment of the applicability of the many naturally occurring small ELM regimes to ITER is the subject of ongoing research [18]. While these assessments have been made historically by examining the operational spaces of small ELM regimes in multiple devices, recent advances in diagnostics now enable comparison of the ELM filamentary structure, which should provide additional insight into the underlying instabilities and improved physics-based extrapolability. In this paper, we present the first comparison of small ELM regimes

in the Alcator C-Mod, the Mega-Amp Spherical Tokamak (MAST) and the National Spherical Torus Experiment (NSTX) devices, both in terms of operational windows and diagnostic signatures.

In Alcator C-Mod, the enhanced  $D_\alpha$  (EDA) regime [19–22] is a high recycling, normally ELM-free regime. A quasi-coherent edge oscillation is responsible for continuous density and impurity transport, preventing radiated power buildup typical of ELM-free H-modes. The EDA H-mode has been shown [13] to evolve into a regime with individual small ELMs at sufficiently high pedestal temperature and/or pedestal  $\beta$  as defined below. Large, more regular type I ELMs have only been observed in shapes with large lower triangularity and small upper triangularity [23]. Type III ELMs, which were not the subject of the joint experiments, occur with low input power or high radiation, and are characterized by low edge electron temperature in C-Mod [24]. In MAST type III ELMs (which are of intermediate size with  $\Delta W/W_{\text{tot}} \sim 1\text{--}3\%$ ,  $\Delta W/W_{\text{ped}} \sim 3\text{--}10\%$ ) were the most common operational regime when these experiments were executed [25], although type I ELMs have dominated more recent experiments. Small ELMs in MAST, which differ from both type I and type III ELMs, were observed in specific circumstances, described in detail below. Finally in NSTX a wide range of ELMs including type I and type III ELMs has been observed [14, 26, 27]. In addition, a small ELM regime, termed type V ELMs, has been shown to have a wide operating window with unique low- $n$  filamentary ELM structure [14]. In the rest of this paper, we first describe the experiments in C-Mod, MAST and NSTX, and then compare the characteristics of these various small ELM regimes in all three devices, with the ultimate goal of determining if there is a common underlying instability.

## 2. Overview of experiments

A true dimensionless comparison matching plasma boundary shape, normalized gyro-radius ( $\rho^*$ ), normalized collisionality ( $\nu^*$ ) and normalized plasma pressure ( $\beta$ ) is not possible between these devices. C-Mod, as a conventional tokamak, has a minimum aspect ratio  $R/a \sim 2.7$ , as compared with the typical aspect ratio range  $\sim 1.3\text{--}1.5$  for the MAST and NSTX spherical tokamaks. In addition the typical C-Mod  $\beta_{\text{ped}}$  is one tenth of the MAST and NSTX values, owing partly to the order of magnitude difference in toroidal field,  $B_t$ , which prevented an overlap in that quantity. Here  $\beta_{\text{ped}} = 4\mu_0 P_e^{\text{ped}}/|B_{\text{ped}}|^2$ , where  $P_e^{\text{ped}}$  is the electron pressure at the top of the pedestal,  $\mu_0$  is the permeability of free space and  $|B_{\text{ped}}|$  is the magnitude of the total magnetic field at the outer midplane pedestal top. On the other hand, poloidal  $\beta$  at the top of the pedestal,  $\beta_{\text{ped}}^{\text{pol}} = 4\mu_0 P_e^{\text{ped}}/|B_{\text{ped}}^{\text{pol}}|^2$ , can be comparable between these devices; here,  $|B_{\text{ped}}^{\text{pol}}|$  is the magnitude of the poloidal magnetic field at the outer midplane pedestal top. This relation assumes that the electron and ion pressures at the top of the pedestal are equal; this assumption is made because ion pressure profiles were not routinely measured in all three devices. Thus, it was decided to match the scaled poloidal cross-sections in the three devices, as shown in figure 1, while trying to also match the edge safety factor  $q_{95}$ . The latter was chosen in part because  $q_{95}$  was observed [28] to be a critical parameter

in establishing the similarity between EDA H-mode in C-Mod and the high recycling steady (HRS) H-mode [29] in JFT-2M. A heating power scan in each device then provided an electron collisionality  $\nu_e^*$  and  $\beta_{\text{ped}}$  scans for determination of the small ELM destabilization threshold conditions.

### 2.1. Alcator C-Mod results

Alcator C-Mod is a compact, high field, diverted tokamak [30, 31] with the following machine parameters: major radius  $R = 0.67$  m, minor radius  $a_m \leq 0.22$  m, plasma current  $I_p \leq 2$  MA, on-axis vacuum toroidal field  $B_t \leq 8$  T, elongation  $\kappa < 1.8$  and typical triangularities in the dominant X-point between 0.4 and 0.6. The device design aspect ratio allows making ITER-like shapes at approximately 1/9 scale. Heating is provided by up to 6 MW of ion cyclotron range of frequencies (ICRF) power, and in the experiments described was absorbed on the H minority fundamental frequencies of 78–80 MHz. The plasmas facing components are made of molybdenum, and boronization is used to mitigate high- $Z$  impurity accumulation and achieve optimum H-mode performance. The upper divertor is outfitted with an in-vessel cryopump for additional pumping, which was active in these discharges.

Measurement of the edge pedestal parameters in this paper is enabled by a high resolution edge Thomson scattering system with 1.3 mm spatial resolution (mapped to the outer midplane) [32, 33]. The ELMs are observed using two gas-puff imaging (GPI) diagnostic systems, which view a local  $D_2$  or He gas puff along the magnetic field line to image the coherent, turbulent structures; both systems view nearly the same outboard midplane region of the pedestal and SOL. One system utilizes an array of localized views that have been coupled to filtered diodes [34]. Its spatial resolution is  $\sim 4$  mm, and it has a  $\sim 500$  kHz frequency response. Signals from this system are shown in figures 5(c) and (d). The second GPI diagnostic is a camera with a maximum framing rate (for these experiments) of  $148\,000$  frames  $s^{-1}$ . The spatial resolution of this system is  $\sim 2$  mm. Snapshots from movies taken using this camera system are shown in figure 6.

The small ELM regime documented in previous Alcator C-Mod experiments [13] was obtained in a lower single null boundary shape with  $I_p = 0.8$  MA,  $B_t = 5.2$  T, safety factor at the 95% flux surface  $q_{95} = 5.5$ , elongation  $\kappa = 1.7$ , lower triangularity  $\delta_L = 0.5$  and magnetic balance parameter  $\delta_r^{\text{sep}} \sim -5$  mm.  $\delta_r^{\text{sep}}$  is defined as the radial distance between the two X-point flux surfaces mapped to the outer midplane. The ion  $B \times \nabla B$  drift was towards the lower X-point. Figure 2 shows the  $D_\alpha$  traces for the discharges in an ICRF power scan, in which small ELMs were observed (red ovals). An apparent ICRF power threshold of  $\sim 3$  MW was required to access small ELMs, which is consistent with thresholds in normalized plasma pressure (i.e.  $\beta_N > 1.3$ ) previously observed (with higher ICRF power) in more typical C-Mod equilibria [13]. Here  $\beta_N = \beta_t B_t a_m / I_p$ , where  $\beta_t$  is the plasma pressure (normalized to the on-axis vacuum toroidal field) from equilibrium reconstructions. In terms of local plasma values, the small ELM threshold value for  $\beta_{\text{ped}}$  was  $\sim 0.3\%$ . The small ELMs were still present at the highest rf power level of 4.5 MW ( $\beta_{\text{ped}} > 0.5\%$ ). The normalized [35]  $\nu_e^*$  range (calculated using  $Z_{\text{eff}} = 1$  here and for other devices) at the top of the pedestal was between 1 and 4 for these discharges.

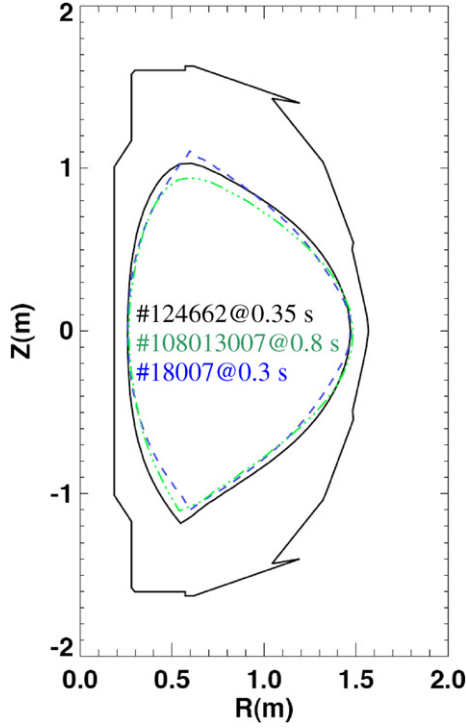


**Figure 1.** Common shape developed for experiment. Colour code: NSTX (black), MAST (blue: dashed) and C-Mod (green: dashed-dotted). The NSTX and C-Mod plots are scaled by 0.96 and 2.8, respectively, and the C-Mod boundary is shifted inwards by 0.19 m.

There was an apparent narrow  $I_p$  access window for small ELM destabilization in the plasma shape used for these experiments: changes of  $\pm 50$  kA from the base value eliminated all signs of small ELMs. In addition, the  $\delta_r^{\text{sep}}$  could be changed only by  $\pm 1$ – $2$  mm before access to the small ELM regime was lost. The small ELM access window in  $\delta$  was also relatively narrow, with lower divertor triangularity  $\delta_L = 0.585 \pm 0.025$ . Note that the narrowness of this access window is not understood. This is shown in figure 3, where the small ELMs can be clearly seen in panel (f), but begin to disappear and/or change character in panels (e) and (g), in which  $\delta_L$  was changed by  $\pm 0.025$ . Note that the upper divertor triangularity  $\delta_U$  dropped from 0.45 to 0.43 as the  $\delta_L$  was increased. The small ELMs were visible on the edge soft x-ray (SXR) emission, fast magnetics and GPI diagnostic [36], although their individual impact on stored energy was indiscernible from the statistical noise on equilibrium reconstructions.

In comparison, large ELMs were seen in C-Mod in the high  $\delta_L \sim 0.75$  shape developed for similarity studies with the JFT-2M device [23] (with  $\delta_U \sim 0.15$ ). The comparison of the boundary shapes needed for small ELM and large ELM access, along with discharge characteristics, is shown in figure 4 for completeness. Note that the  $T_e$  at the 95% flux surface and  $\beta_N$  are comparable, despite the dramatically different  $D_\alpha$  signatures in panels (e) and (f).

In edge imaging diagnostics, the ELMs are coincident with the observation of filamentary structures that have some commonalities with electrostatic turbulence filaments. The latter filaments have long parallel wavelength and finite poloidal cross-sections, and have been studied extensively in

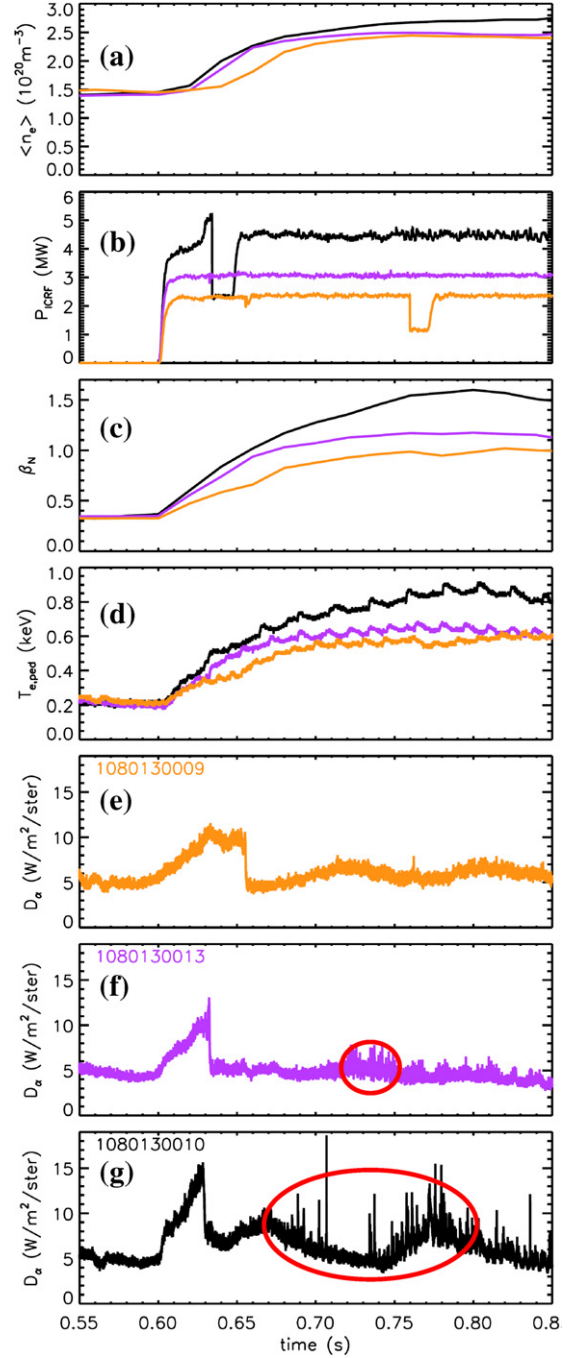


**Figure 2.** ICRF heating power scan in Alcator C-Mod with (a) line-average density  $\bar{n}_e$ , (b) ICRF power, (c) plasma normalized pressure, (d) pedestal  $T_e$  from the ECE diagnostic at  $\psi_N \sim 0.82$ , and (e)–(g)  $D_\alpha$  emission from each discharge. Small ELMs are present in (f) and (g).

C-Mod, both in L-mode and EDA H-mode discharges [36–40]. In L-mode, the turbulence filaments were imaged just inside the separatrix (because of the radial location of  $D_\alpha$  light), and they propagated in the electron diamagnetic drift direction [37]. In H-mode the  $D_\alpha$  light emission was from filaments in the SOL, and these propagated in the ion diamagnetic drift direction.

While a detailed comparison of the small ELM filaments and turbulence filaments is beyond the scope of this paper, subtle differences can be observed between the GPI images of

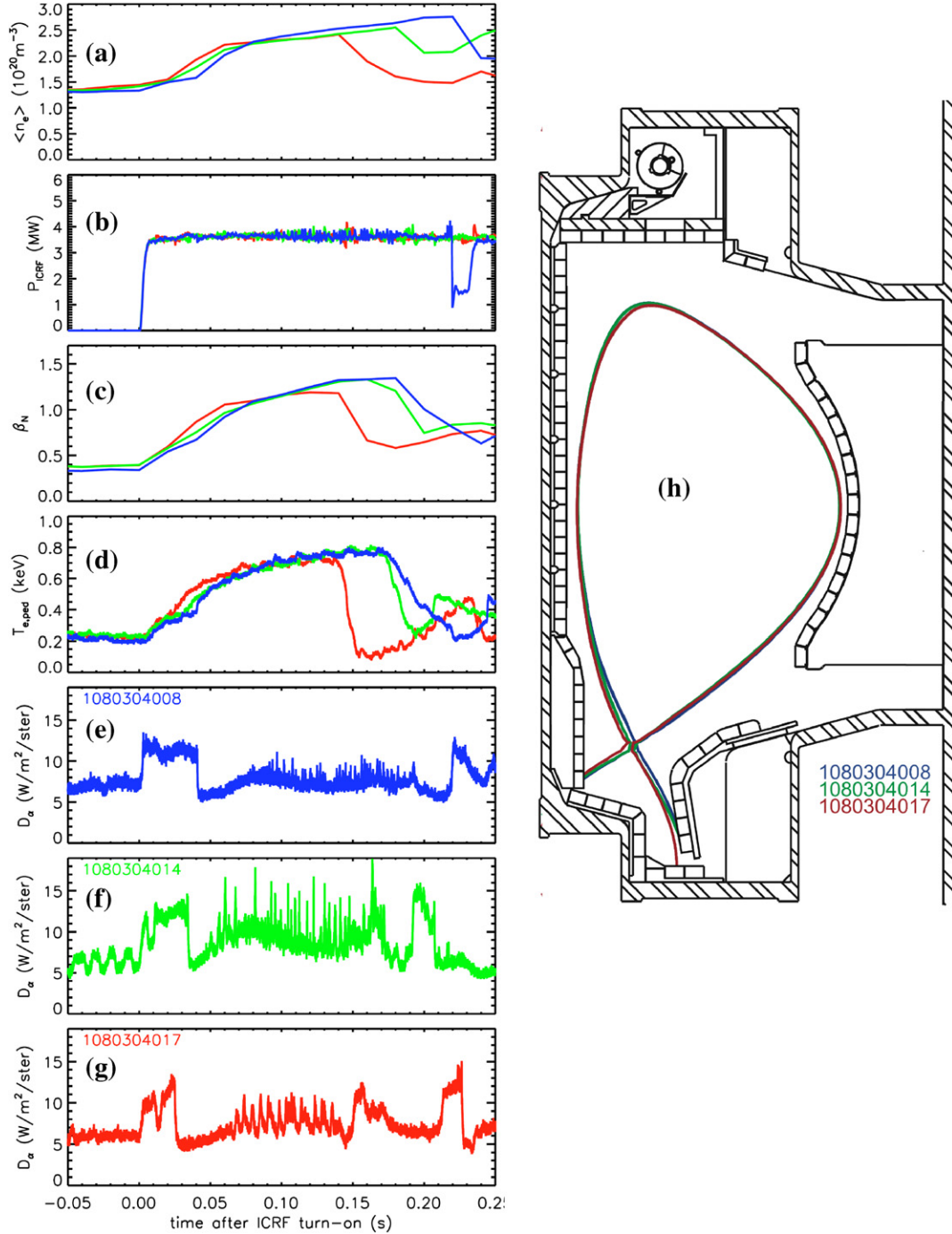


**Figure 3.** Lower divertor triangularity scan in Alcator C-Mod with (a) line-average density  $\bar{n}_e$ , (b) ICRF power, (c) plasma normalized pressure, (d) pedestal  $T_e$  from the ECE diagnostic at  $\psi_N \sim 0.84$ , and (e)–(g)  $D_\alpha$  emission from three different  $\delta_L$  from 0.56 to 0.61, with boundary shapes shown in (h). Small ELMs are prominent in (f).

these two phenomena. Figure 5 shows three small ELMs in the shaded regions (panel (a)), along with edge SXR emission (panel (b)), GPI  $D_\alpha$  emission from the pedestal (panel (c)) and far SOL regions (panel (d)). Each ELM correlates with a drop in the edge SXR emission, which is not observed for electrostatic turbulence filaments.

While individual filaments can be seen in panel (d), the small ELMs appear as bursts of filaments that are accompanied by a decrease in the pedestal  $D_\alpha$  emission (panel (c)). We note that multiple filaments are also observed in large type I ELMs,

which can consist of primary and secondary filaments [23]. In addition, the movement of the ELM filaments is mainly radial, with possibly a slight downward component, i.e. which would be consistent with the ion diamagnetic drift direction or co- $I_p$  direction, and in the same direction as the turbulence filaments. Figure 6 shows the 2D images from the GPI diagnostic at the two times indicated in figure 5. The inter-ELM turbulence filamentation is barely visible in panel (a), while the bright coherent structure is a field-aligned view of the filamentary structure associated with the small ELM in panel (c).

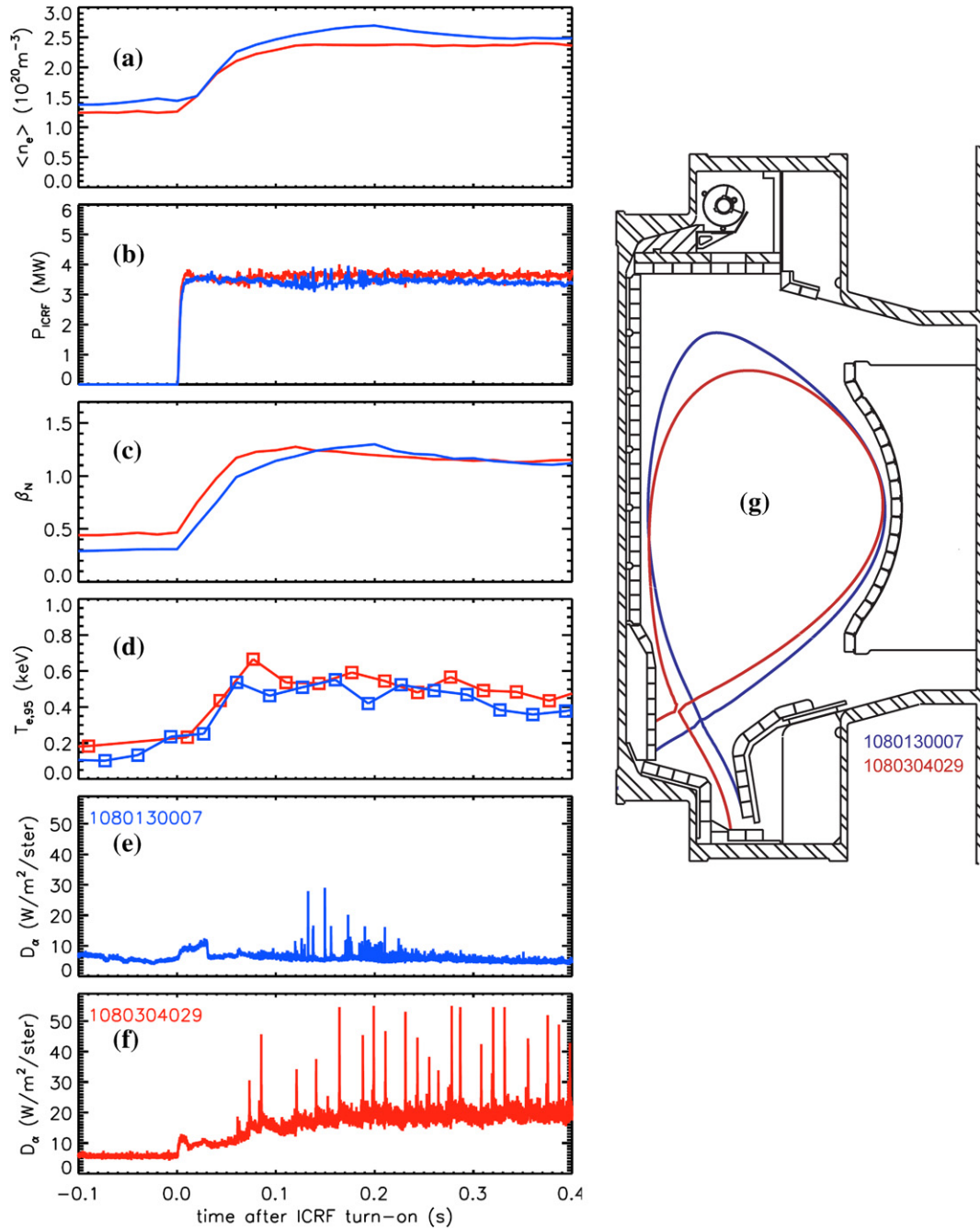


**Figure 4.** Small ELM and large ELM discharge comparison in Alcator C-Mod with (a) line-average density  $\bar{n}_e$ , (b) ICRF power, (c) plasma normalized pressure, (d) pedestal  $T_e$  from the Thomson scattering diagnostic at  $\psi_N \sim 0.95$ , and (e)–(f)  $D_\alpha$  emission from small ELM and large ELM discharges, with boundary shapes shown in (g).

## 2.2. MAST results

MAST is a medium-sized spherical tokamak with the following machine parameters:  $R = 0.85$  m,  $a_m \leq 0.65$  m, plasma current  $I_p \leq 1.4$  MA,  $B_t \leq 0.6$  T,  $\kappa \leq 2.5$ , with operation typically in double-null diverted configuration [41]. The typical aspect ratio  $R/a_m$  was  $\sim 1.5$ . Heating is provided by up to 4 MW of neutral beam injection (NBI). The plasmas facing components are made of graphite. The wall conditioning programme consists of high temperature baking, periodic boronization and helium glow discharge cleaning (HeGDC) between plasma discharges.

The edge pedestal parameters were measured with a 16 channel, 200 Hz Thomson scattering system with  $\sim 10$  mm spatial resolution at the outer midplane [42]. Imaging of the plasma filament structure is provided by a fast ( $10 \mu\text{s}$  exposure), wide-angle visible camera that has been successfully used for ELM and L-mode filament studies [43, 44].

In the MAST device, a variety of ELMs has been observed [45], including the small ELMs in these experiments with double-null boundary shapes with  $I_p = 0.7$  MA,  $B_t = 0.59$  T,  $q_{95} = 5.5$ ,  $\kappa = 1.9$ ,  $\delta = 0.43$ ,  $\delta_r^{\text{sep}} \sim 0$  mm, and with the ion  $B \times \nabla B$  drift towards the lower X-point. A power scan

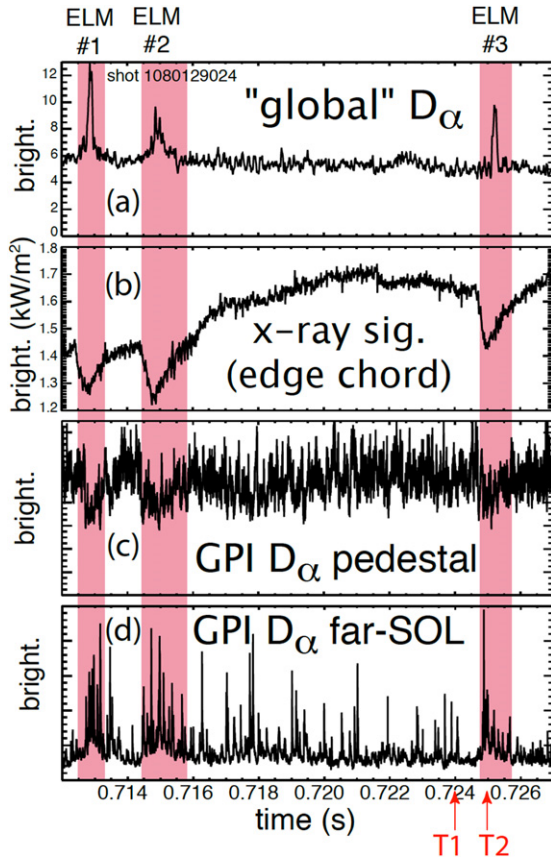


**Figure 5.** Alcator C-Mod data showing 3 small ELMs: the time histories from (a) a ‘global’  $D_\alpha$  signal (actually a radial view through the plasma), (b) a SXR signal from a chord passing through the plasma edge (note suppressed 0), (c) a  $D_\alpha$  signal from a  $\sim 4$  mm spot near the top of the pedestal, and (d) a  $D_\alpha$  signal from a  $\sim 4$  mm spot in the far SOL. (c) and (d) are from the GPI diagnostic viewing near the outboard midplane. These views and those of (a) and (b) are at different toroidal and poloidal locations. Also shown are the times ‘T1’ and ‘T2’ of the spatially resolved GPI snapshots shown in figure 6.

was conducted to determine the operational window for these small ELMs. Figure 7 displays the discharges from the power scan, along with plasma stored energy and  $D_\alpha$  emission. Type III ELMs were observed in panels 7(c) and (f) and the early time of panel 7(g); large type I ELMs can be seen at the later times in panel 7(g).

The small ELMs are best seen as the small oscillations in panel 7(f) between 0.29 and 0.33 s (red oval). However, careful inspection of the data showed that they were present between the type III ELMs in panels 7(c)–(e) also, but clearly absent when type I ELMs appeared, in 7g. The small ELMs themselves have no measurable impact on stored energy. In terms of collisionality, the small ELMs occurred over a wide range:  $1.5 < \nu_e^* < 20$ , inter-mixed with type III ELMs in the upper range while completely disappearing at the lower range as type I ELMs appeared.

The pedestal profiles between ELMs from the discharges in figure 7 were analysed to produce an operational existence plot for small and type I ELMs, which is shown in figure 8. A few additional discharges with reduced  $B_t = 0.52$  T were also included to vary the relationship between  $\beta_{ped}$  and  $\nu_e^*$ .

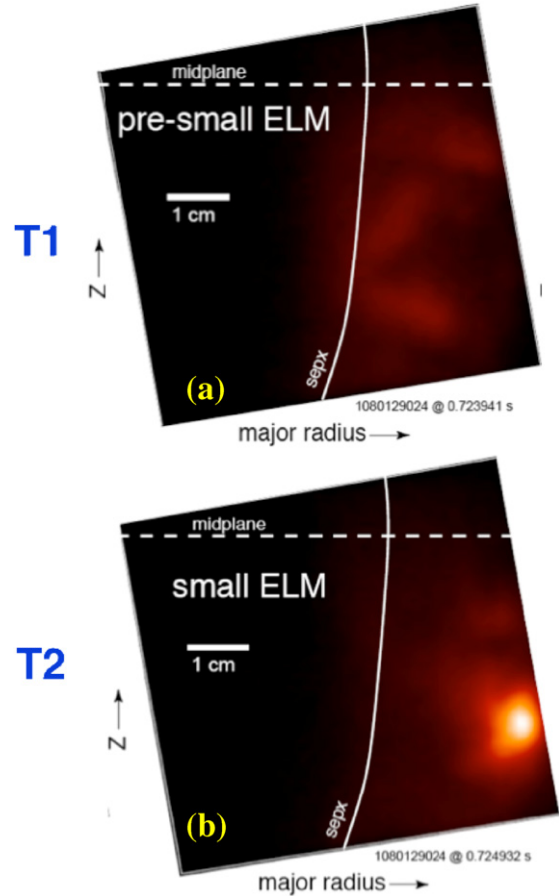


**Figure 6.** Alcator C-Mod snapshots from the GPI diagnostic, showing (a) inter-ELM turbulence, and (b) small ELM filament from the two time slices in figure 5.

Figure 8 shows that small ELMs were present for each of these conditions except for the red triangles, i.e. that there is an upper limit of  $\beta_{ped} \leq 3.5\%$  for observation of small ELMs. Analysis of additional MAST discharges [45] with type III and type IV ELMs has shown that the upper limits in  $\beta_{ped}$  for those ELMs are 5% and 7.5%, respectively, with the type IV ELMs existing at low  $\nu_e^*$  [46].

We attempted to obtain H-mode discharges with  $\delta_r^{sep} < -0.6$  cm, i.e. in a shape that more strongly favoured the lower X-point for closer comparison with the other devices; those shapes are more conducive for observation of the type V ELMs observed in NSTX. However, H-mode could not be realized with further reduced  $\delta_r^{sep}$  in the MAST plasmas, consistent with previous MAST observations of reduced power threshold in a double-null shape [47]. For completeness, we note that in other lower single null shapes with reduced plasma volume and with reduced  $\delta_U$  and  $\delta_r^{sep} < -4$  cm, H-mode is readily achieved; however, no small ELMs have been observed in those discharges so far.

The small ELMs have a high- $n$  structure as clearly observed with the wide-angle view visible camera, as shown in figure 9. A regular banded, filamentary structure is observed in panel 9(b) during the ELM growth in panel 9(a). There are typically 20–30 filaments that have a substantial length parallel to the magnetic field, and a few cm cross section perpendicular to the magnetic field. In comparison, 10–20 filaments are

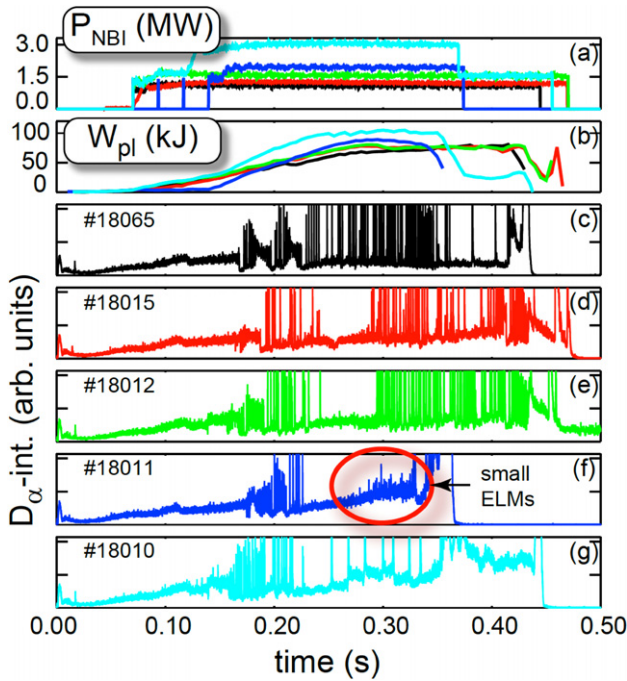


**Figure 7.** NBI heating power scan in MAST discharges. The NBI power is shown in (a), and plasma stored energy in (b), and the divertor  $D_\alpha$  characteristics of each discharges in the NBI scans in (c)–(g). Small ELMs are prominent in (f), absent in (g), and inter-mixed with type III ELMs in (c)–(e).

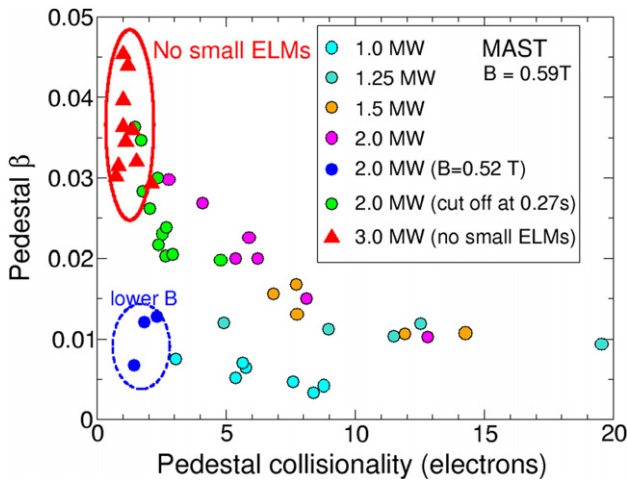


**Figure 8.** Operational space of ELM types in MAST from discharges in figure 7 and a few additional discharges at lower  $B_t = 0.52$  T, in  $\beta_{ped}$  and  $\nu_e^*$  space. The individual discharges from the NBI scan have been colour-coded. Small ELMs are present in every data point except for the red triangles.

typically observed [48] during type I ELMs. The filament propagation is in the same direction as the toroidal rotation of the pedestal; this represents the ion diamagnetic drift direction as long as the filaments are attached to the plasma. This propagation direction is similar to the inter-ELM turbulence filaments on MAST and C-Mod. The dynamics of these small ELMs differ from large ELMs [43, 49] and inter-ELM filaments on MAST in that most of the filaments from these small ELMs do not detach from the plasma, i.e. they do not accelerate radially towards the outer wall.

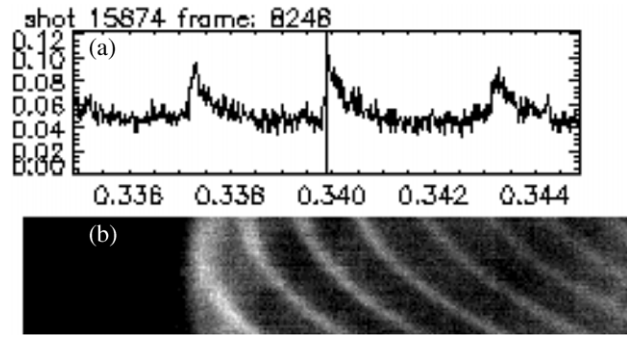


**Figure 9.** ELM images from a visible camera in MAST: (a)  $D_\alpha$  trace during small ELMs, and (b) a portion of a wide-angle view of the plasma, showing a large number of discrete filaments. The number of filaments in small ELMs is roughly 100% more than in ordinary type I ELMs.

### 2.3. NSTX results

NSTX is a medium-sized spherical tokamak with the following machine parameters:  $R = 0.85$  m,  $a_m < 0.67$  m, plasma current  $I_p \leq 1.4$  MA,  $B_t \leq 0.55$  T, a possible range of  $\kappa$  from 1.7 to 3, and triangularities between 0.3 and 0.8 [50]. The typical aspect ratio  $R/a_m$  was  $\sim 1.4$ . Heating is provided by up to 7.4 MW of NBI and up to 6 MW of high harmonic fast wave (HHFW) power, although this set of experiments used NBI exclusively. The plasma facing components are made of graphite. We note that while NSTX typically uses lithium wall coatings to further improve plasma performance [51, 52] and suppress [53, 54] type I ELMs, these experiments were conducted with boronization and inter-shot HeGDC at the beginning of the campaign before any lithium had been evaporated in the vacuum vessel.

The edge pedestal parameters were measured with a 30 channel, 60 Hz Thomson scattering system with  $\sim 10$ – $15$  mm spatial resolution at the outer midplane [55]. Edge turbulence with a GPI system analogous to the Alcator C-Mod design, with up to 250 kHz frame rate and with spatial resolution down to 5 mm [56].

In the NSTX device, two distinct classes of small ELMs were identified in this set of experiments, all with the ion  $B \times \nabla B$  drift towards the lower X-point. In near double-null boundary shapes that slightly favour the lower divertor and are otherwise similar to the MAST device shapes ( $I_p = 0.9$  MA,  $B_t = 0.42$  T,  $q_{95} = 5.5$ ,  $\kappa = 1.8$ ,  $\delta = 0.5$ ,  $-2$  mm  $< \delta_r^{sep} < -6$  mm), an intermediate- $n$  small ELM has been identified in a narrow heating power window. We have tentatively classified this ELM as type II, owing to its appearance in boundary shapes very close to a double-null configuration [6, 7]. Figure 10(d) shows the occurrence of this type II ELM regime with a red oval; type III ELMs are apparent in panel 10(e) and type I ELMs are the large perturbations in panels 10(c)–(d). Additional details on the observed characteristics of type II ELMs are given in section 3, when common features of the ELMs from the three devices are compared.

In discharges that more strongly favour the lower divertor ( $\delta_r^{sep} \sim -15$  mm, reduced X-point height required for H-mode access), the more common type V ELM regime [57, 58] with single or double filaments in a broad  $\beta_{ped}$  window, was observed. At the highest heating power in panel 10(h), type I ELMs are inter-mixed with type V ELMs. Note that H-mode

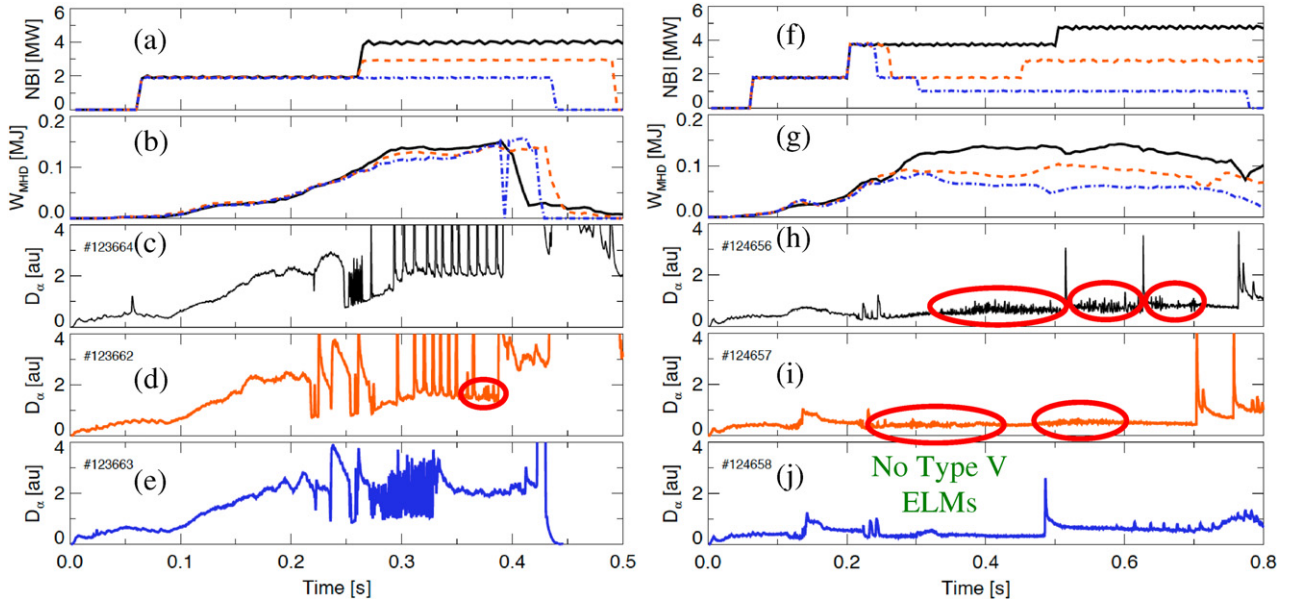


**Figure 10.** NBI heating power scan in NSTX discharges. The left panels (a)–(e) were taken with  $\delta_r^{\text{sep}} = -0.6$  cm, whereas the right panels (f)–(j) were with  $\delta_r^{\text{sep}} = -1.5$  cm and a lower X-point height. The oval highlights the small (type II) ELMs in (d) and the ovals in (h) and (i) highlight type V ELMs.

access was not possible with  $q_{95} = 5.5$  at large  $\delta_r^{\text{sep}}$ ; thus, the discharges in panels 10(f)–(j) were obtained with  $q_{95}$  between 9 and 10. We also obtained an H-mode power scan with  $q_{95} \sim 8$  in a different set of experiments, which confirmed that the type V ELM access window is independent of  $q_{95}$  as previously reported [27].

The differences in ELM structure between the type II ELMs in panel 10(d) and type V ELMs in panels 10(g)–(h) are clearly seen in the data from the GPI diagnostic [56]. The field-aligned GPI diagnostic views a gas puff near the plasma boundary to produce a 23 cm  $\times$  23 cm radial (x-axis) and vertical (y-axis) cross section of the emission (figure 11(a)); in the absence of the external gas puff, the entire filament structure is sometimes visible. Figure 11(b) shows that the type II ELM has multiple filaments in the GPI view, indicating a higher equivalent poloidal/toroidal mode number. The filaments clearly propagate downwards poloidally, i.e. qualitatively consistent with the ion diamagnetic drift direction and the toroidal rotation direction of the pedestal, as observed for the C-Mod and MAST small ELMs. In contrast, the type V ELMs have a single/double filamentary structure as shown in figure 11(c) (note that no external gas puff was used here), and clearly propagate upwards, i.e. in the electron diamagnetic drift or counter- $I_p$  direction. These type V ELM filaments have been shown to persist for up to 1 ms, with an apparent toroidal propagation speed of 10 km s $^{-1}$  [57]. In addition, the type V ELM typically spawns secondary turbulence filaments (not shown) [59]. Note that the primary filament of the type V ELM often does not detach from the plasma, as observed for the MAST small ELM. Neither of the small NSTX ELMs discussed here has a measurable impact on plasma stored energy, i.e.  $\Delta W/W_{\text{tot}} \leq 0.01$  ( $\Delta W/W_{\text{ped}} \leq 0.03$ ).

### 3. Discussion and summary

Having tentatively classified one set of ELMs from NSTX as type II, we begin this section with a brief review of

the characteristics of type II ELMs; additional background information on type II ELM regimes is given in [6, 7]. In the original observation [5] of type II ELMs from DIII-D, the large amplitude  $D_\alpha$  signatures were replaced with smaller  $D_\alpha$  spikes when the  $\kappa$  and/or  $\delta$  were increased. This reduction in ELM amplitude was attributed to an improved access to the second stability regime. In ASDEX-Upgrade, type II ELMs were observed [6] in discharges with  $-0.5 \text{ cm} \leq \delta_r^{\text{sep}} \leq 0$  cm, i.e. very close to double-null configuration, and only at the highest possible  $\delta \sim 0.4$ . These discharges maintained  $\delta$  and  $\kappa$  to within a few %, demonstrating that  $\delta_r^{\text{sep}}$  was the controlling operational parameter. An increased broadband fluctuation was observed in discharges' phases with type II ELMs, and a coherent pre-cursor with frequency  $\sim 30$  kHz was identified. Subsequent experiments [7, 9] in JET also accessed type II ELMs in configurations near double-null, with increased broadband fluctuations as in ASDEX-Upgrade. In JET, however, mixed type I and II ELM regimes are commonly observed. These observations can be used to distinguish type II ELMs from 'grassy' ELMs in that 'grassy' ELMs were observed [10] with large  $|\delta_r^{\text{sep}}|$ ; in the latter case, high  $\delta$  was found to be the important operational parameter for access, in addition to the observed  $\beta_p$  threshold. There was no enhancement of broadband turbulence in the 'grassy' ELM operation in JT-60U, in contrast to the type II ELMs regimes in ASDEX-Upgrade and JET.

To examine the data from C-Mod, MAST, and NSTX in context with the type II and 'grassy' ELM characteristics described above, the operating windows for pedestal parameters were determined in these three devices. The edge  $n_e$  and  $T_e$  profiles from each device were fit with a modified hyperbolic tangent function to obtain the pedestal values, from which  $\beta_{\text{ped}}$  and  $v_e^*$  were computed [27, 33, 47]. The pedestal operational space windows from the three devices for the periods with and without small ELMs are displayed in figure 12.

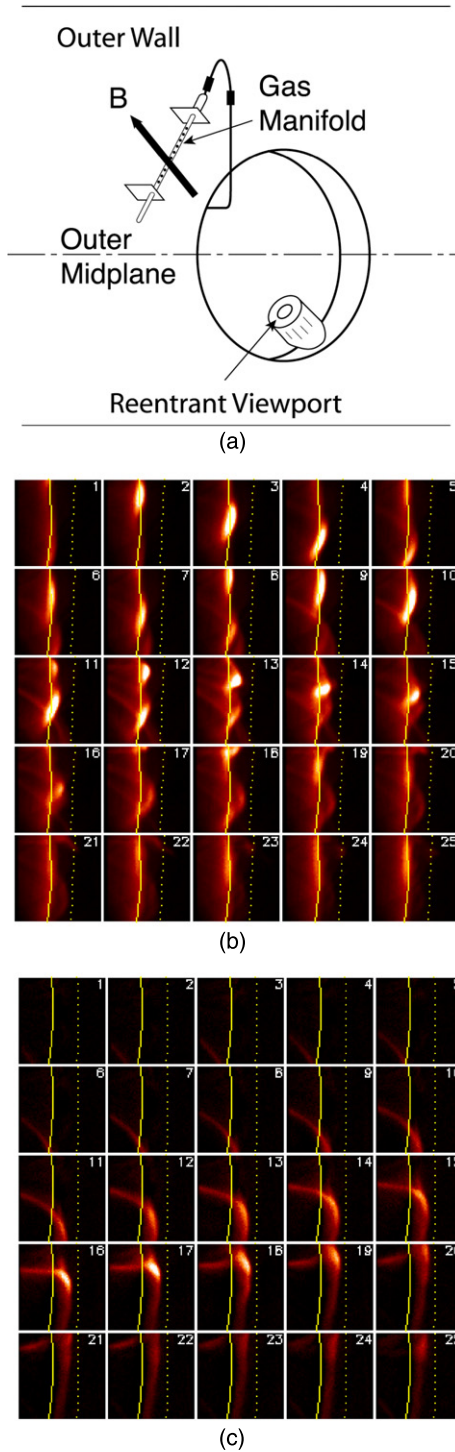


**Figure 11.** (a) GPI setup on NSTX, showing camera view of gas manifold along  $B$ , (b) NSTX type II ELM images with GPI from #123656,  $t = 339.217$  at  $8.1 \mu\text{s}$  per frame. (c) NSTX type V ELM images from the same view but without a local gas puff, from #119318, starting at  $t = 668.277$  at  $8.1 \mu\text{s}$  per frame. The solid line represents the EFIT separatrix, and the dashed line the shadow of the RF antenna.

The C-Mod data (triangles) show that the small ELMs were observed in the higher  $\beta_{\text{ped}}$  range of the data, i.e. no small ELMs were observed below  $\beta_{\text{ped}} < 0.3\%$ , and there was no direct  $\nu_e^*$  dependence. Consistent with previous observations [28], there are no data points in these EDA H-modes with

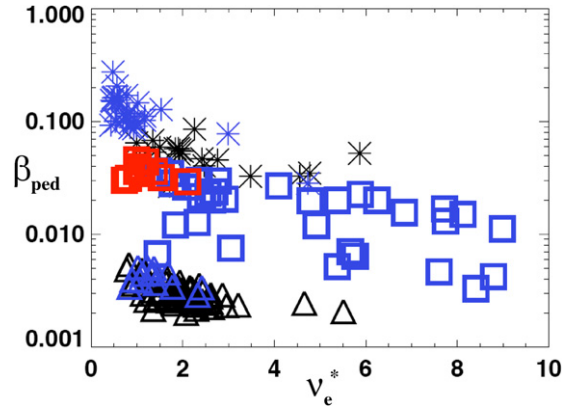


**Figure 12.** Small ELM edge operational space in Alcator C-Mod (triangles), MAST (squares) and NSTX (stars—type V ELMs only). Black signifies no small ELMs, blue signifies that small ELMs were observed and red signifies that only large ELMs observed (no small ELMs mixed in). The C-Mod data are from EDA H-modes, the MAST data from small ELMs in double-null configuration, and the NSTX data from type V ELMs H-mode. The NSTX type II ELM operational window is shown in figure 13.

$\nu_e^* < 1$ , and so we cannot make conclusive statements about the lower bound in collisionality for these small ELMs. The MAST data (squares) show a broad  $\beta_{\text{ped}}$  range from 0.3% to 3.5%, with the small ELMs disappearing when  $\beta_{\text{ped}} > 3.5\%$  and when  $\nu_e^* < 2$ , when only type I ELMs were observed. The NSTX type V ELM data show a somewhat higher threshold, i.e.  $\beta_{\text{ped}} > 3\%$  is needed for access. The type V ELMs are present even at the highest  $\beta_{\text{ped}} \sim 20\%$ , albeit between a mixed ELM regime interspersed between type I ELMs. On the other hand, the type II ELMs in NSTX appear in a very narrow operational window, and have an upper  $\beta_{\text{ped}}$  limit, as in MAST.

Thus, one general feature of these small ELM scenarios is that access occurs in apparent  $\beta_{\text{ped}}$  windows, although the details differ between the devices. As mentioned above, because of the difference in aspect ratio between C-Mod and MAST/NSTX, different definitions of  $\beta$  (referenced to average  $B_t$  or pedestal  $B_t$ ) scale differently in these devices. The observed difference in operational windows shown in figure 12 indicates that either the  $\beta_{\text{ped}}$  definition used is not the controlling parameter for access to these small ELM regimes or the threshold itself depends on  $R/a$ . There is, notably, no common scaling with  $\nu_e^*$  when for both type II and type V ELMs. Concerning type II ELM windows from all three devices, the data are not inconsistent with a required  $\nu_e^* \geq 1$ .

An initial attempt to improve the overlap of the pedestal operating window data is shown in figure 13, where the pedestal  $\beta$  is normalized by the poloidal field, rather than the total magnetic field; this normalization is termed  $\beta_{\text{ped}}^{\text{pol}}$ . Note that we plot the NSTX type II ELM operational window as a singular point in figure 13(c) because the access window is so narrow. Figure 13 shows that when  $\beta_{\text{ped}}^{\text{pol}}$  reaches a value between 10% and 15%, small ELMs are observed in the three devices, although in MAST (C-Mod), the  $\beta_{\text{ped}}^{\text{pol}}$  value of  $\sim 12\%$  is an upper (lower) bound. It is also clear that  $\beta_{\text{ped}}^{\text{pol}}$  is not the precise organizing quantity, but it may nevertheless be closely related to the critical parameter(s). The differences in the operational windows might also be related to other shape

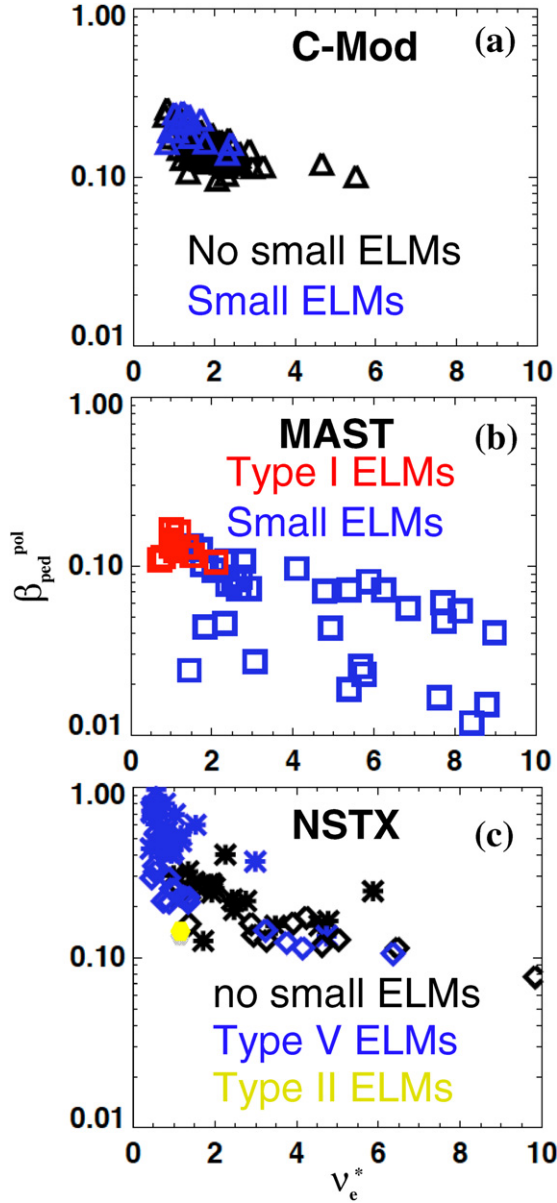


**Figure 13.** Small ELM operational space for the (a) C-Mod, (b) MAST and (c) NSTX in  $\beta_{\text{ped}}^{\text{pol}}$  and  $v_e^*$  space. The same data depicted in figure 12 are shown here. Black signifies no small ELMs, blue signifies that small ELMs were observed, and red signifies that only large ELMs observed (no small ELMs mixed in). The type II ELM space in NSTX is also indicated in (c) by the yellow octagon. The stars in (c) were obtained at  $q_{95} = 10$ , and diamonds were obtained at  $q_{95} = 8$ .

parameters, such as the  $\delta_r^{\text{sep}}$  or the upper divertor triangularity, or minor differences in actual pedestal  $Z_{\text{eff}}$  since all of these calculations used  $Z_{\text{eff}} = 1$  in computing  $v_e^*$ .

The clear upper bound in  $\beta_{\text{ped}}^{\text{pol}}$  for the small ELM access in MAST appears similar to the NSTX type II ELMs, but clearly not the NSTX type V ELMs. New data from C-Mod at higher  $\beta_{\text{ped}}^{\text{pol}}$  are needed to determine if there is an upper limit for small ELM access, i.e. an upper limit cannot be ruled out, which means that the small ELMs in C-Mod, MAST and the type II ELMs in NSTX could well have common underlying physics. Partly due to these similarities and the fact that these small

ELMs were observed in a near double-null configuration in all three devices, we also classify the C-Mod and MAST small ELMs as type II. On the other hand, the type V ELMs in NSTX appear to be different instabilities.

The visible camera images of ELMs show some common features with inter-ELM turbulence filaments, but with important distinctions in each machine. In C-Mod, the small ELMs affect the emission in the pedestal and generate bursts of filaments that subsequently detach from the main plasma and propagate radially. In MAST, the small ELMs have a periodic structure with more filaments than larger ELMs, and most of the filaments do not detach from the plasma. In both C-Mod and MAST, the propagation of the ELM filaments and turbulence filaments is consistent with the ion diamagnetic drift direction, i.e. the toroidal rotation direction at the pedestal top. In NSTX, the type V ELMs contain one or two filaments, but these propagate in the counter  $I_p$  direction consistent with electron diamagnetic drift direction, i.e. opposite to the type II ELMs discussed above and normal turbulence filaments. For reference, the  $\beta_{\text{ped}}$  and  $v_e^*$  ranges in the NSTX type II ELM discharges were between 6% and 9%, and 0.8 and 2.2, respectively. Thus we submit (1) that the type V ELMs are indeed distinct from the C-Mod and MAST small ELMs, and (2) that the NSTX type II ELMs have a poloidal propagation direction similar to the small ELMs on C-Mod and MAST.

One straightforward conclusion from these studies is that small ELMs can indeed have different toroidal mode structures and operational windows, even within a single device. Thus there may be multiple scenarios by which small ELMs could be achieved naturally in ITER. In addition, subtle changes in shape, particularly the magnetic balance as characterized by  $\delta_r^{\text{sep}}$ , can modify access to these small ELM scenarios.

Stability analysis of these small ELMs is complicated because the resulting profile relaxation is quite subtle, obviating stability comparisons based on the ‘before’ and ‘after’ ELM profiles, although some progress has been reported from other devices [60]. Ideal MHD calculations of the NSTX discharges with type V ELMs previously indicated [57] stability to low- $n$  and high- $n$  ideal modes, possibly pointing to the need for resistive MHD calculations, which are commencing. Ideal MHD calculations for MAST indicate that the edge profiles are far from either the peeling or ballooning boundaries. Similar calculations for C-Mod are commencing, and will help identify whether the small ELMs are, as in previous C-Mod experiments, at the peeling–ballooning boundary as anticipated for type II ELMs.

## Acknowledgments

This research was supported in part by the US Department of Energy Contracts DE-AC05-00OR22725, DE-FC02-99ER54512, DE-FG02-04ER54767 and DE-AC02-09CH11466, and partly by the United Kingdom Engineering and Physical Sciences Research Council under grant EP/G003955 and the European Communities under the contract of Association between EURATOM and CCFE. The views and opinions expressed herein do not necessarily reflect those of the European Commission. We gratefully acknowledge the contribution of the technical and operations staff from Alcator C-Mod, MAST and NSTX. In addition, we

acknowledge the valuable discussion and support from the ITPA pedestal physics working group, as well as valuable critique from the referees.

## References

- [1] Wagner F. *et al* 1982 *Phys. Rev. Lett.* **49** 1408
- [2] Zohm H. *et al* 1994 *Plasma Phys. Control. Fusion* **36** A129
- [3] Zohm H. 1996 *Plasma Phys. Control. Fusion* **38** 105
- [4] Loarte A. *et al* 2003 *J. Nucl. Mater.* **313–316** 962
- [5] Ozeki T. *et al* 1990 *Nucl. Fusion* **30** 1425
- [6] Stober J., M. Maraschek and Conway G.D. 2001 *Nucl. Fusion* **41** 1123
- [7] Saibene G. *et al* 2005 *Nucl. Fusion* **45** 297
- [8] Leonard A.W., Osborne T.H., Fenstermacher M.E. and Mahdavi M.A. 2001 *J. Nucl. Mater.* **290–293** 1097
- [9] Saibene G. *et al* 2002 *Plasma Phys. Control. Fusion* **44** 1769
- [10] Kamada Y. *et al* 2000 *Plasma Phys. Control. Fusion* **42** A247
- [11] Oyama N. *et al* 2005 *Nucl. Fusion* **45** 871
- [12] Kamada y. *et al* 1996 *Plasma Phys. Control. Fusion* **38** 1387
- [13] Mossessian D.A. *et al* 2003 *Phys. Plasmas* **10** 1720
- [14] Maingi R. *et al* 2005 *Nucl. Fusion* **45** 264
- [15] Loarte A. *et al* 2007 *Phys. Scr.* **T128** 222
- [16] Evans T.E. *et al* 2004 *Phys. Rev. Lett.* **92** 235003
- [17] Lang P.T. *et al* 2005 *Nucl. Fusion* **45** 502
- [18] Oyama N. *et al* 2006 *Plasma Phys. Control. Fusion* **48** A171
- [19] Takase Y. *et al* 1997 *Phys. Plasmas* **4** 1647
- [20] Greenwald M. *et al* 1999 *Phys. Plasmas* **6** 1943
- [21] Greenwald M., Basse N. and Bonoli P. 2007 *Fusion Sci. Technol.* **51** 266
- [22] Hughes J.W., Hubbard A.E. and Mossessian D.A. 2007 *Fusion Sci. Technol.* **51** 317
- [23] Terry J.L. *et al* 2007 *J. Nucl. Mater.* **363–365** 994
- [24] Hubbard A.E. *et al* 1998 *Plasma Phys. Control. Fusion* **40** 689
- [25] Kirk A. *et al* 2004 *Plasma Phys. Control. Fusion* **46** 551
- [26] Maingi R. *et al* 2005 *J. Nucl. Mater.* **337–339** 727
- [27] Maingi R. *et al* 2005 *Nucl. Fusion* **45** 1066
- [28] Hubbard A.E. *et al* 2006 *Plasma Phys. Control. Fusion* **48** A121
- [29] Kamiya K. *et al* 2004 *Plasma Phys. Control. Fusion* **46** A157
- [30] Hutchinson I.H. *et al* 1994 *Phys. Plasmas* **1** 1511
- [31] Marmar E. *et al* 2009 *Nucl. Fusion* **49** 104014
- [32] Hughes J.W. *et al* 2001 *Rev. Sci. Instrum.* **72** 1107
- [33] Hughes J.W. *et al* 2006 *Phys. Plasmas* **13** 056103
- [34] Terry J.L. *et al* 2001 *J. Nucl. Mater.* **290–293** 757
- [35] Sauter O., Angioni C. and Lin-Liu Y.R. 1999 *Phys. Plasmas* **6** 2834
- [36] Terry J.L. *et al* 2003 *Phys. Plasmas* **10** 1739
- [37] Cziegler I., Terry J.L., Hughes J.W. and LaBombard B. 2010 *Phys. Plasmas* **17** 056120
- [38] Grulke O., Terry J.L., LaBombard B. and Zweben S.J. 2006 *Phys. Plasmas* **13** 012306
- [39] Zweben S.J. *et al* 2006 *Phys. Plasmas* **13** 056114
- [40] Zweben S.J. *et al* 2009 *Phys. Plasmas* **16** 082505
- [41] Lloyd B. *et al* 2004 *Plasma Phys. Control. Fusion* **46** B477
- [42] Scannell R. *et al* 2007 *Plasma Phys. Control. Fusion* **49** 1431
- [43] Kirk A. *et al* 2006 *Phys. Rev. Lett.* **96** 185001
- [44] Kirk A. *et al* 2006 *Plasma Phys. Control. Fusion* **48** B433
- [45] Kirk A. *et al* 2009 *Plasma Phys. Control. Fusion* **51** 065016
- [46] Meyer H. *et al* 2009 *Nucl. Fusion* **49** 104017
- [47] Meyer H. *et al* 2005 *Plasma Phys. Control. Fusion* **47** 843
- [48] Kirk A. *et al* 2005 *Plasma Phys. Control. Fusion* **47** 995
- [49] Kirk A. *et al* 2004 *Phys. Rev. Lett.* **92** 245002
- [50] Ono M. *et al* 2000 *Nucl. Fusion* **40** 557
- [51] Bell M.G. *et al* 2009 *Plasma Phys. Control. Fusion* **51** 124054
- [52] Kugel H.W. *et al* 2008 *Phys. Plasmas* **15** 056118
- [53] Maingi R. *et al* 2009 *Phys. Rev. Lett.* **103** 075001
- [54] Mansfield D.K. *et al* 2009 *J. Nucl. Mater.* **390–391** 764
- [55] LeBlanc B.P. *et al* 2003 *Rev. Sci. Instrum.* **74** 1659
- [56] Maqueda R.J. *et al* 2001 *Rev. Sci. Instrum.* **72** 931
- [57] Maingi R. *et al* 2006 *Phys. Plasmas* **13** 092510
- [58] Maqueda R.J. *et al* 2007 *J. Nucl. Mater.* **363–365** 1000
- [59] Maqueda R.J., Maingi R., Ahn J.-W. and the NSTX Team 2009 *J. Nucl. Mater.* **390–391** 843
- [60] Saarelma S. *et al* 2009 *Plasma Phys. Control. Fusion* **51** 035001